

High-resolution, cross-well reflection imaging: Potential and technical difficulties

Spyros K. Lazaratos*, James W. Rector III[‡], Jerry M. Harris*, and Mark Van Schaack*

ABSTRACT

The case study presented in this paper demonstrates that reflections can be found in high-frequency cross-well data. These reflections can be enhanced by a processing sequence similar to the one applied to VSP data to produce very high-resolution images. Vertical resolution of the order of 3–5 ft (1–1.5 m) for well distances of a few hundred feet is potentially feasible.

Although this study produced a good tie between the cross-well reflection image and the sonic log, our research also illustrated some of the technical difficulties associated with cross-well reflection imaging. Specifically, we found that the signal-to-noise ratio of the image decreases as the distance between the imaged reflection points and the wells increases, and that aliased tube waves as well as shear and converted waves were the main components of the noise. We also observed that interpretation of wide-angle reflections might be misleading, since these events are significantly stretched, both horizontally and vertically, during imaging. Improvements are required both in data acquisition (denser data collection, more fold, smaller angles of incidence) and processing/imaging (optimal use of fold) to make cross-well reflection imaging useful. Still, the quality of these preliminary results, produced from a single gather of aliased data, indicates the promise of the approach.

INTRODUCTION

In most cross-well imaging studies, especially in those dealing with real cross-well data, the direct-arrival traveltimes have been inverted to produce seismic velocities in the region between wells. Direct-arrival traveltimes are definitely a robust observation that should be used whenever available. However, direct arrivals represent only a small

fraction of the total information contained in the data. Processing the full waveform has been advocated by several authors as a means of achieving resolution higher than what can be obtained with traveltime measurements only. A variety of imaging approaches have been proposed, ranging from VSP-CDP mapping (Baker and Harris, 1984; Iverson, 1988; Abdalla et al., 1990), to migration (Hu et al., 1988), to acoustic diffraction tomography (Devaney, 1984; Harris, 1987; Miller et al., 1987; Wu and Toksöz, 1987; Lo et al., 1988; Woodward, 1989; Pratt and Worthington, 1990a) or elastic diffraction tomography (Beydoun et al., 1989; Beydoun and Mendes, 1989; Pratt and Worthington, 1990b).

Although there has been a significant number of contributions to the theory of waveform inversion (or reflection imaging) as it applies to the cross-well geometry, relatively few real data studies have been published (Baker and Harris, 1984; Iverson, 1988; Beydoun et al., 1989; Abdalla et al., 1990; Becquey et al., 1991). These studies have illustrated important imaging principles and have identified some of the prominent events present in the data, but have not demonstrated high correlation with log-based synthetics.

The case study presented here shows that a good correlation between the cross-well reflection image and the sonic log can be achieved, and this reliable correlation enables us to understand the nature of the cross-well reflected wavefield. In general, geophysicists know how to interpret seismic reflection sections, but they are not familiar with seismic images produced with frequencies of a few kHz. We are going to see that even the finest features shown on the logs, thin layers with thicknesses of 3 to 5 ft (1 to 1.5 m), can be significant reflectors at these frequencies.

This study demonstrates that the piezoelectric bender transducer is an appropriate source/receiver for cross-well reflection imaging at frequencies of a few kHz and well separations of a few hundred feet. The bender source is also shown to generate shear (direct, reflected, and converted) waves with a radiation pattern qualitatively similar to what is predicted by theory (White, 1983; Lee and Balch, 1982). In

Manuscript received by the Editor December 23, 1992; revised manuscript received January 28, 1993.

*Dept. of Geophysics, Stanford University, Stanford, CA 94305.

[‡]Formerly Stanford University; presently Department of Engineering Geoscience, University of California, Berkeley, CA 94720.

© 1993 Society of Exploration Geophysicists. All rights reserved.

our data example, shear-wave arrivals were not evident in the raw data, but were revealed after appropriate processing.

Besides demonstrating the high-resolution potential of the cross-well reflection imaging approach, this paper discusses some of the technical difficulties that have to be overcome for this technology to become a useful tool. Further noise attenuation by multichannel filtering and stacking is necessary to reliably image away from the wells, and advances are needed in data acquisition to sample the wavefield correctly (Rector et al., 1992) and at the processing/imaging stage to optimally use the fold.

SITE AND DATA DESCRIPTION

The cross-well data used in this study were collected at British Petroleum's test site located southwest of San Antonio near Devine, Texas. The site and data acquisition technique for a different data set collected at the same site were described by Harris (1988). Two cased boreholes—Wilson 2 and Wilson 4—were used. Each borehole is about 3000 ft (915 m) deep and their separation is 330 ft (100 m). A sketch of the geology and the sonic logs for Wilson 2 and Wilson 4 are shown in Figure 1. The two logs indicate lateral homogeneity, even for most of the finer scale features.

The cylindrical piezoelectric bender transducer described by Balogh et al. (1988) was used as both a downhole source and a receiver. The radiated wavelet was one period of a 2 kHz sinusoid. Seismic waves with significant energy in the frequency band of about 300 Hz to 4000 Hz were recorded.

A single common receiver gather—a total of 133 traces—comprised the data set to be studied. The receiver was located at a depth of 2340 ft (715 m) in the Wilson 2 well and

source positions in Wilson 4 covered a range of depths from 2125 ft (650 m) down to 2785 ft (850 m). The direct raypath coverage for this single fan of data is schematically shown by the shaded area in Figure 1. The depth spacing between successive source positions—the vertical separation between two successive traces—was 5 ft (1.5 m). The raw data, with a 50 ms AGC applied, are shown in Figure 2.

Looking at the data we can easily identify a clean direct compressional arrival. The abrupt changes in the slope of the direct arrival in the lower part of the section are caused by velocity contrasts between the Eagle Ford shale, the Buda limestone, and the Del Rio clay. Data of this quality would certainly be appropriate for traveltime tomography, since it is obvious that the first breaks can be picked accurately and unambiguously. However, reflections are hardly visible. We can identify only one reflection event, which originates at the top of the Eagle Ford shale at a depth of about 2540 ft (775 m). A raypath for this reflection event is shown schematically in Figure 1. This one event is essentially the only reflection visible in the raw data.

This quick inspection of the data reveals a major reason why cross-well reflection imaging has, up to now, been far less popular with real data than has traveltime tomography; we can see the direct arrivals in the raw data but, in most cases, we cannot see reflections.

Two groups of strong linear events—a group with positive slope and another with negative slope—are also observed in Figure 2. These events are related to tube waves generated in the source well and, for data collected with the piezoelectric transducer, they represent a dominant type of coherent noise. In this case they appear to be very narrow band and

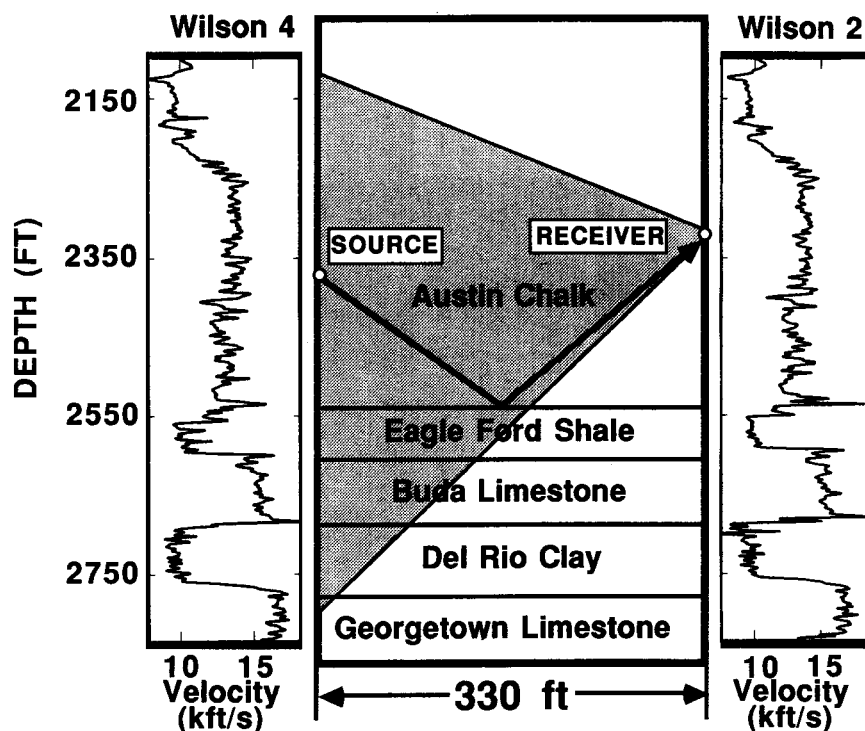


FIG. 1. Sketch of the geology and data acquisition geometry at the Devine test site.

essentially obscure everything following the direct arrival. Tube waves are also generated in the receiver well, but they do not have linear moveout in common receiver gathers and for this reason they are not easily identifiable in this particular data example. Receiver well tube waves will appear as linear events in common source gathers.

Because tube waves have a well defined linear moveout they can potentially be removed from the data (with f - k filtering for example), provided they are adequately sampled in space. The problem though is that because the tube waves are very slow, they are rarely properly sampled in cross-well data recording. In this particular case, for example, the 5-ft (1.5-m) vertical sampling interval in the source well created a Nyquist frequency of approximately 475 Hz for the tube waves. So, for all frequencies higher than 475 Hz, the tube waves were aliased.

Notice that the 5-ft (1.5-m) vertical sampling interval used here is actually smaller than what is typically used for traveltimes tomography applications. Still, this spatial sampling is not small enough for full-waveform processing at the high frequencies generated by the piezoelectric transducer. So it is already clear that compared to traveltimes tomography cross-well reflection imaging requires us to collect data at a much finer vertical source/receiver spacing, if we are to filter out tube-wave noise. Additional reasons why full-waveform processing requires a much finer spatial sampling are discussed by Rector et al. (1992a).

DATA PROCESSING

Cross-well geometry is similar to offset VSP geometry. For this reason, we decided to process this data set in

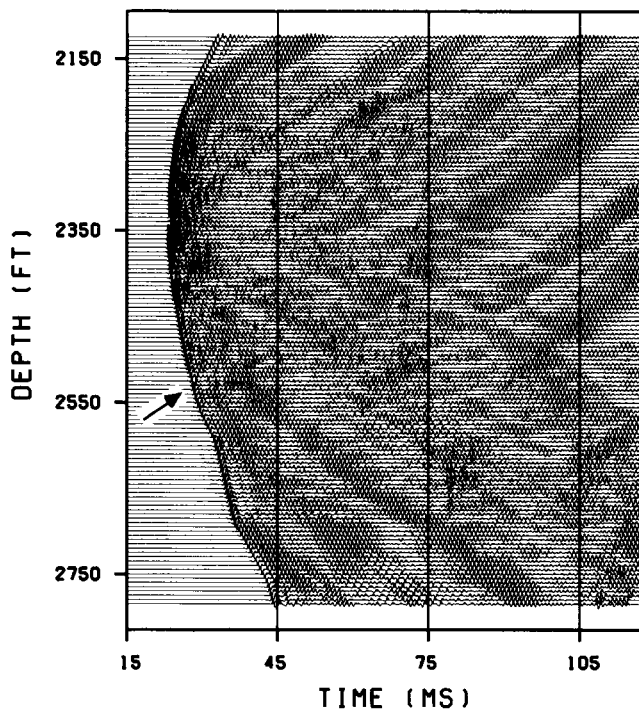


FIG. 2. Common-receiver gather. The arrow identifies a P -wave reflection originating at a depth of about 2540 ft.

essentially the same way that VSP data are commonly processed (Hardage, 1985). A flow chart of the processing sequence is shown in Figure 3.

Spectral whitening is done as the first processing step to attenuate the spectral peak associated with the strong narrow-band tube waves. This whitening was accomplished by using predictive deconvolution with a prediction distance of 1.5 ms, operator length of 30 ms, and 1 percent white noise. The whole trace was used for the design of the operator. To preserve relative phase between traces, the autocorrelation used to derive the operator was obtained as a mix of 50 adjacent trace autocorrelations. The result of this procedure is shown in Figure 4. The data are displayed with the same AGC as the data in Figure 2. We can see that whitening the spectrum had the effect of compressing the tube-wave wavelet and improving the signal-to-noise ratio for many events that were previously hidden below the tube waves. Observe, for example, the hyperbolic event that can be seen at shallow depths between about 50 and 70 ms. This is a shear direct arrival that was invisible in the raw data.

After whitening, the data were band-pass filtered from 300 to 2000 Hz. This filtering was done to avoid aliasing the shear and shear-converted reflections, which as we are going to see a little bit later, are also present in the data. Next, the direct arrival was picked, aligned, amplitude balanced, enhanced with an 11-trace lateral mix, and subtracted from the data. The enhanced direct arrival is shown in Figure 5a. A sequence of reverberations occurs after the two main lobes of the direct arrival wavelet. These events seem to be related to the geology

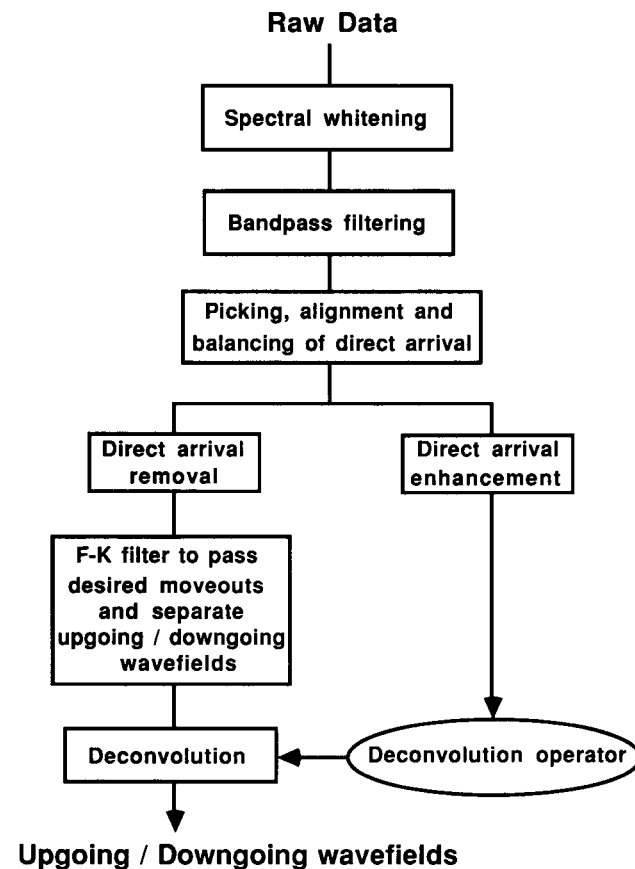


FIG. 3. Processing sequence flow chart.

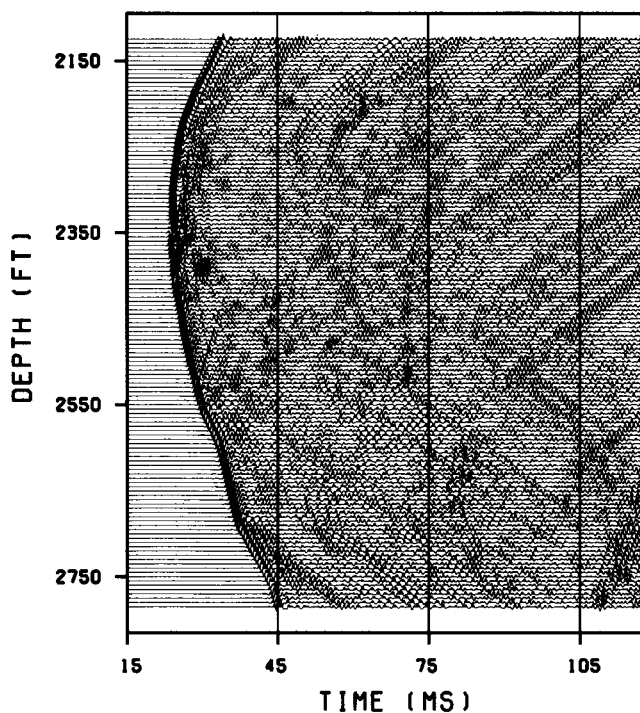


FIG. 4. Data after spectral whitening.

immediately around the receiver, but their generation mechanism is not exactly known at the moment. They are removed from the data after the subtraction of the direct arrival.

The enhanced direct arrival provides a reliable estimate of the wavelet that is received after propagating through the interwell space and includes the effects of anelastic attenuation, radiation pattern and short period interbed multiples. This wavelet defines the incident source wavefield, which is then convolved with the reflectivity of the earth to produce the reflection arrivals. However, the direct arrival is a reliable estimate of the reflection wavelet only for the area close to the receiver well since reflections coming from this area follow raypaths that are close to the direct arrival raypaths. For reflections produced away from the wells, this correspondence between travel paths is no longer true. So, away from the wells, we lose the advantage that we have in zero-offset VSP—the ability to measure the earth's response at every depth level and to use this response for deterministic deconvolution. As with offset VSP, in the cross-well geometry the wavelet might have to be statistically rather than deterministically estimated.

After the direct arrival was removed, the data were f - k filtered. The purpose of this filtering was to pass events with desired moveouts (rejecting P - S converted reflections) and to separate the data into upgoing and downgoing wavefields. The upgoing wavefield contains primary reflections from interfaces below the receiver, and the downgoing wavefield contains primary reflections from interfaces above the receiver. Both upgoing and downgoing wavefields were deconvolved. The enhanced direct arrival was used to estimate the deconvolution operator. An operator was designed that converted the direct arrival wavelet, shown in Figure 5a, to

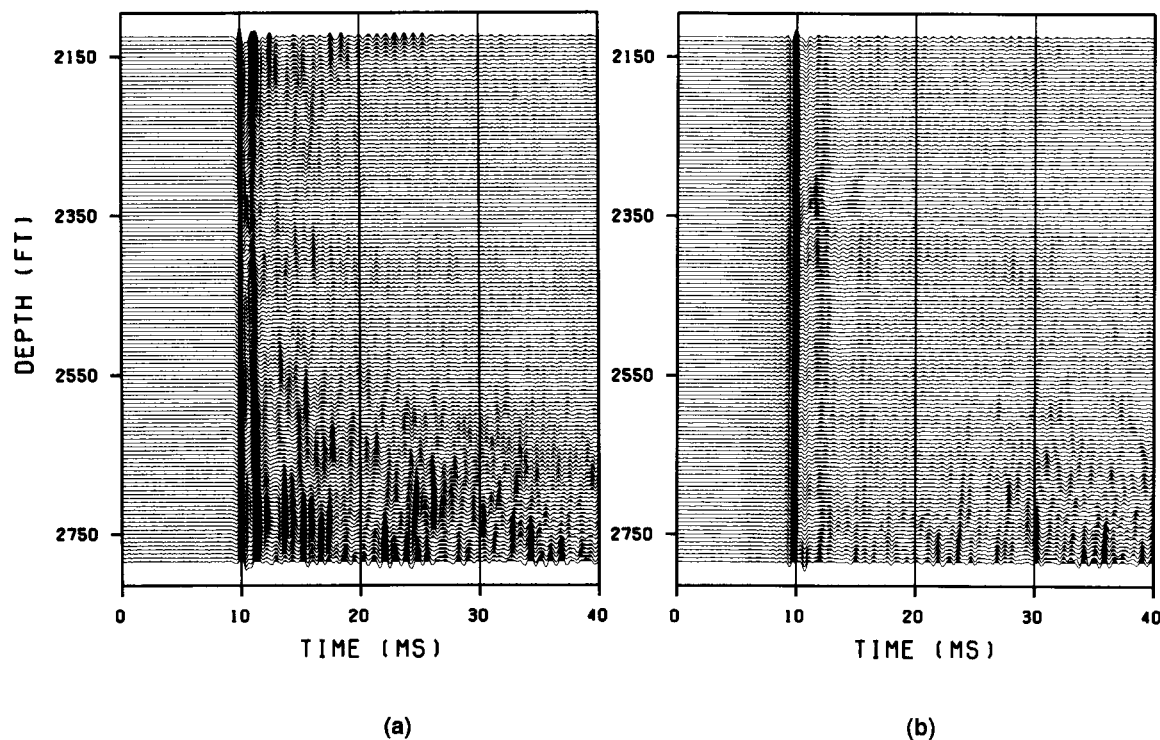


FIG. 5. (a) Enhanced direct arrival. (b) Deconvolved direct arrival.

a more compressed form, shown in Figure 5b. The same operator was applied to the upgoing and downgoing wavefields. In this case we used spiking deconvolution, with an operator length of 10 ms and a design gate of 20 ms. The objective of this deconvolution was to compress the wavelet, and the deconvolution operator did not significantly reduce multiples. The approach used in VSP—using deconvolution operators designed from the downgoing wavefield to eliminate multiples in the upgoing wavefield—is not effective here (Rector et al., Scheduled for publication in January 1994). Upgoing and downgoing cross-well wavefields contain both primaries and multiples, which is unlike VSP where primaries can only be found in the upgoing wavefield. The reason the VSP approach works is that we have the same timing and amplitude relationships between direct arrival and multiples in the downgoing wavefield that we have between primaries and multiples in the upgoing wavefield. These same relationships do not exist for the cross-well geometry.

The upgoing and downgoing wavefields, after deconvolution, are shown in Figure 6. The processing revealed a large number of events that were invisible in the raw data. Many of them are primary P to P reflections. It is obvious though that there is still a lot of noise present in the data. The largest noise contribution comes from the tube waves, which as discussed before, cannot be effectively removed by our processing due to spatial aliasing.

SHEAR WAVES IN THE PIEZOELECTRIC BENDER WAVEFIELD

It is difficult to identify shear waves in the raw data, even though we have seen some evidence of a shear direct arrival after the spectral whitening of the data (Figure 4). However appropriate processing reveals significant shear waves as is

documented in Figure 7. This display was produced by f - k filtering the data to attenuate higher apparent velocity P -wave reflections, followed by band-pass filtering from 300 to 900 Hz. The strongest event in this display is the shear direct arrival. Notice the abrupt changes in its slope at the lower part of the section due to the ray bending inside the Eagle Ford shale, Buda limestone, and Del Rio clay. We observed similar effects for the direct compressional wave.

The piezoelectric bender source and receiver are not clamped to the borehole wall. Originally, the source radiates into the borehole fluid, which supports only compressional waves. At the borehole wall, some of this energy converts to shear body waves that propagate to the receiver well, convert back to fluid-borne compressional energy, and are recorded. The fact that the shear wavefield is relatively stronger in a lower frequency band (300–900 Hz) might be due to a combination of lower shear-wave quality factor and larger shear-wave traveltimes (larger number of wavelengths for the same frequency and propagation distance).

The shear wave has a shadow zone in the area exactly opposite the receiver in the depth range around 2350 ft, which is probably caused by the shear-wave radiation patterns of the piezoelectric bender source and receiver transducers. Theory (White, 1983; Lee and Balch, 1982) predicts a shear-wave amplitude distribution sharply peaked at an angle of 45 degrees from the horizontal that falls off rapidly toward the horizontal.

In Figure 7 we can also identify P - to S -converted reflections and S to S reflections. The presence of these modes in the wavefield of the piezoelectric bender suggests that we could use this type of source/receiver for multiple-mode imaging of reservoirs.

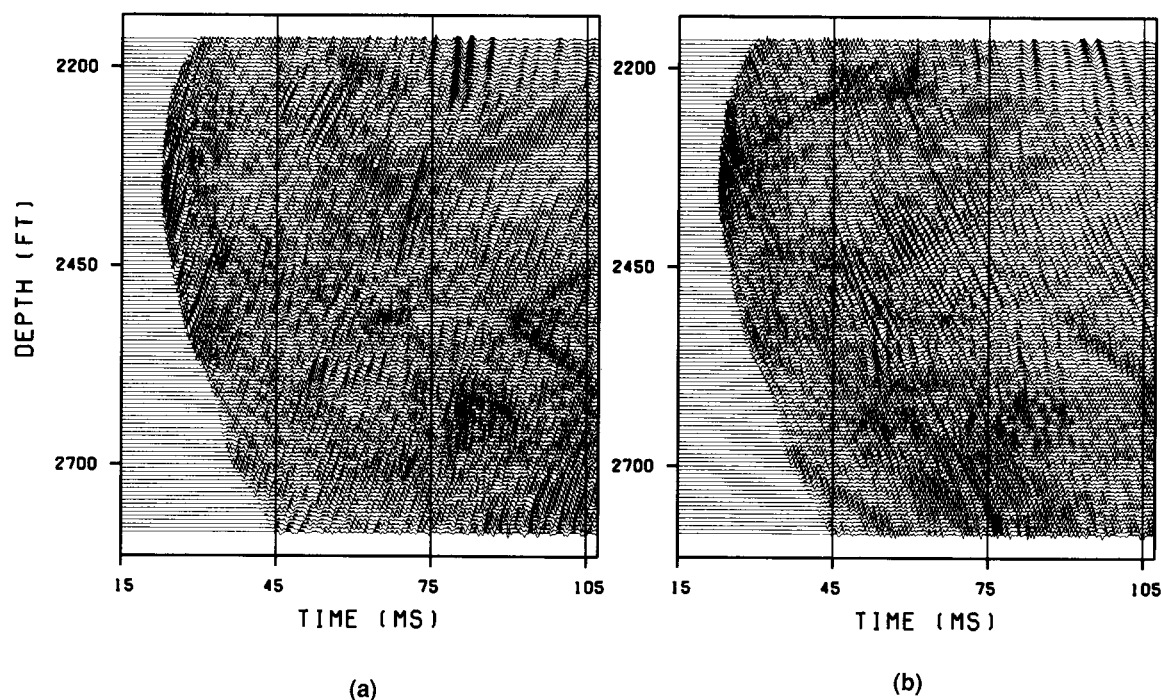


FIG. 6. (a) Upgoing wavefield. (b) Downgoing wavefield.

All the different modes are sources of coherent noise, and each one can degrade the quality of the desired P - to P -reflection image. Wavefield separation can be partially achieved based on moveout differences and time separability between the compressional and shear arrivals, but perfect separation is seldom realized with single-component data.

IMAGING-ANALYSIS OF RESULTS

To produce a depth section from our data, we first need to define a velocity model. Correct imaging at depth always requires an accurate velocity model, but for cross-well geometry, the correct velocity model is particularly significant since we are dealing with wide-angle reflections. Small traveltime errors can easily misposition the reflectors at depth or produce artificial dips.

The velocity model used for imaging is shown in Figure 8. It is a one-dimensional (1-D) isotropic model that was defined by interactively matching the direct-arrival travel-times in a layer-stripping fashion. As we can see in panel (b), the traveltime fit provided by this model is excellent.

A comparison of the two logs indicates that the 1-D assumption is adequate for this site. It has been documented (Harris, 1988; Onishi and Harris, 1991; Miller and Chapman, 1991) that the Del Rio clay and Eagle Ford shale are anisotropic. As we can see in Figure 8, the velocities that fit the cross-well traveltimes for this gather are very close to the vertical well log velocities for these two layers. This agreement between vertical and cross-well velocities can easily be explained. Since the receiver for this gather is significantly above the known anisotropic layers, the rays through these layers are close to the vertical and the effective cross-well velocities are close to the vertical velocities. Since we are

dealing with rays that have similar incidence angles through the anisotropic layers, anisotropy is not really affecting our results. Anisotropy would certainly be a problem if we tried to find a single velocity model that fits the traveltimes from gathers with varying incidence angles through the anisotropic layers.

The enhanced upgoing and downgoing primary P to P reflections (Figure 6) were used to image the area between wells. The imaging algorithm used was a variation of the VSP-CDP mapping algorithm (Wyatt and Wyatt, 1984). To stress the fact that the algorithm is being used for cross-well reflection imaging, its name might have to be changed to XSP-CDP (cross-well seismic profile to common depth point) mapping (Abdalla et al., 1990). This algorithm maps every data point to a possible reflection point based on reflection point locations and traveltimes calculated by ray tracing.

The upgoing and downgoing wavefields are mapped, using the XSP-CDP mapping algorithm, to produce two images of the interwell area. One image is made from the upgoing reflections and the other from the downgoing reflections. Using upgoing reflections, we image reflectors below the receiver, and using downgoing reflections, we image reflectors above the receiver. Thus, images produced from upgoing and downgoing reflections represent different parts of the subsurface as shown schematically in Figure 9. To summarize, we separate our cross-well common-receiver gather into two parts—upgoing and downgoing wavefields—and treat each one of them like a VSP survey. In this way, we end up with the equivalent of two VSPs, a regular one (upgoing primary reflections) and one turned upside-down (downgoing primary reflections).

Another important point is made in Figure 9. For reflection points close to the source well, the reflection traveltimes are close to the direct arrival traveltimes. Consequently, reflections from the area close to the source well can be

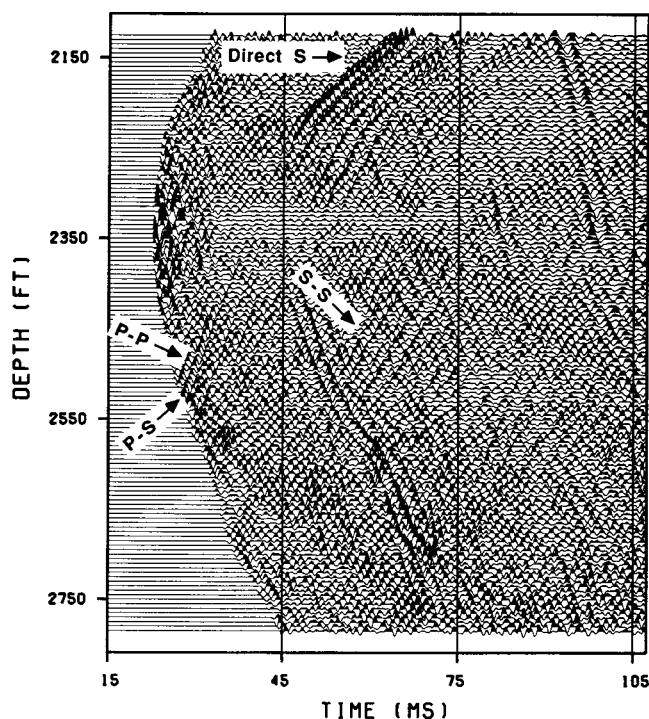


FIG. 7. Enhanced shear arrivals.

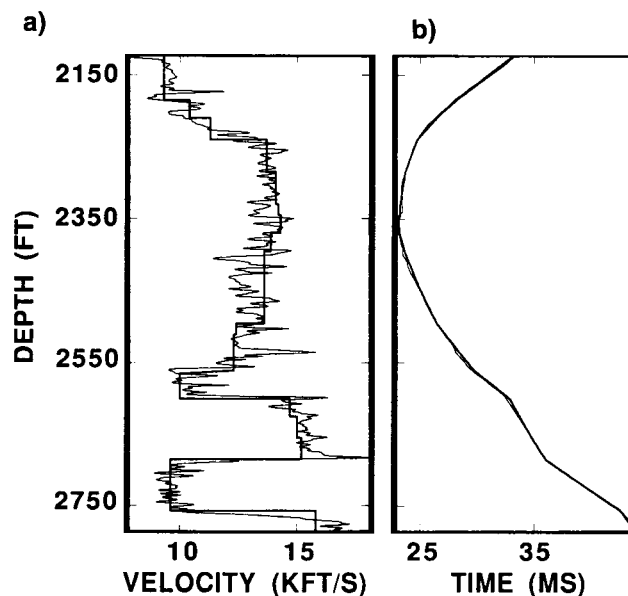


FIG. 8. (a) Velocity model compared to the Wilson 4 sonic log. (b) Fit between picked (thin line) and calculated (thick line) traveltimes.

found in the early part of our data. A simple inspection of Figure 6 indicates that these are the parts of the data where the signal-to-noise ratio seems to be higher and the reflection events seem to be more continuous. There are good reasons why this is happening. As we look deeper into the data (larger traveltimes), the reflection points move away from the source well and geometric spreading for the reflections is increasing. Also, the reflection raypaths form larger angles with the horizontal which causes the reflections to get weaker because of the radiation pattern of the piezoelectric bender for P -waves (maximum in the horizontal direction dropping to a minimum—equal to about 1/3 the maximum—in the vertical direction). Thus, as we move deeper into the data, away from the direct arrival, the reflections are getting weaker, because of both geometric spreading and radiation pattern effects. On the other hand, the tube waves—a major noise contribution—do not experience any geometric spreading or any attenuation related to the radiation pattern. Also, similar to VSP data, while the early part of the data is relatively free of multiples, the later parts contain many multiples. In addition, the shear-wave direct arrival (Figure 7) and associated reflections and conversions occur at later times. So, as we move to later times, the P to P primary reflections get weaker and the noise (tube waves, multiples, shear arrivals) gets stronger. For similar reasons, the signal-to-noise ratio also decreases as we image depths much larger (upgoing reflections) or much smaller (downgoing reflections) than the source/receiver depth.

The conclusion from the above discussion is that the most reliable part of the images is the portion close to the source well and in a range of depths around the source/receiver depth. To further enhance the reflections in this optimal part of the image space and examine the tie of the images to the

log, a procedure similar to what in VSP is called a corridor stack was applied. A 30-ft lateral mix was first applied to the images. A 50-ft part adjacent to the source well was then extracted to form a corridor. Two corridors were produced—one from the upgoing and one from the downgoing reflections.

Imaging close to the well

The imaging results are shown in Figure 10. The sonic log for the source well (Wilson 4) is also shown on the same figure. There are also two synthetic seismograms: one for the frequency range of our experiment (300–2000 Hz) and one for typical surface seismic frequencies (10–60 Hz).

The 10–60 Hz synthetic was calculated as a normal incidence seismogram. The reflectivity series—derived from the sonic log—was convolved with a band-limited (10–60 Hz) wavelet and the resulting trace was converted from time to depth, based on the sonic log velocities.

The 300–2000 Hz synthetic is not a normal incidence seismogram. It was calculated as follows. First, the sonic log was blocked at a very fine scale [layer thickness was of the order of 1 ft (0.3 m)]. Then, synthetic data were generated for the blocked model using the VESPA modeling software of Sierra Geophysics, which is based on a discrete wave-number method (Apsel, 1979). Densities were calculated from compressional velocities based on Gardner's relationship: $density = 0.23 * (velocity)^{0.25}$. Although density logs were available, they were not used for the calculation of the synthetic in this study. This was done to avoid generating artifacts in the synthetic response because of the imperfect alignment of the short wavelength features of the velocity and density logs. Although not addressed here, the optimal way to block and combine well logs to generate synthetics for the very high frequencies used in cross-well seismics will be an important issue for more detailed studies. Currently, the well log measurements are averaged, because of the construction of the tool, over an interval of about 3 ft (1 m), and this distance is a significant portion of our wavelength. Consequently, the short wavelength features that we observe on the logs might not always be reliable enough to compare with cross-well seismic. In any case, our goal here was mainly to identify and correlate events rather than to interpret the relative amplitudes.

A V_P/V_S ratio of 1.87, estimated from the compressional- and shear-wave direct arrival traveltimes in the Austin chalk, was used for the synthetic calculation. Shear-wave picks of the full waveform sonic were not used for the same reasons the density log was not used. For the generation of the synthetic, the recording geometry was simulated exactly to incorporate the effects of oblique incidence. The wavelet was derived from the data after deconvolution (Figure 5). The final synthetic data contained only primary reflections. A separate synthetic, containing only the direct arrival, was also generated and used to balance the amplitude of the reflections. This balancing was similar to the procedure applied to the real data (see related discussion in the data processing section), and its purpose was to compensate for the effects of geometric spreading and radiation pattern. The synthetic primary reflection data were then mapped with the XSP-CDP mapping program. The velocity model used for

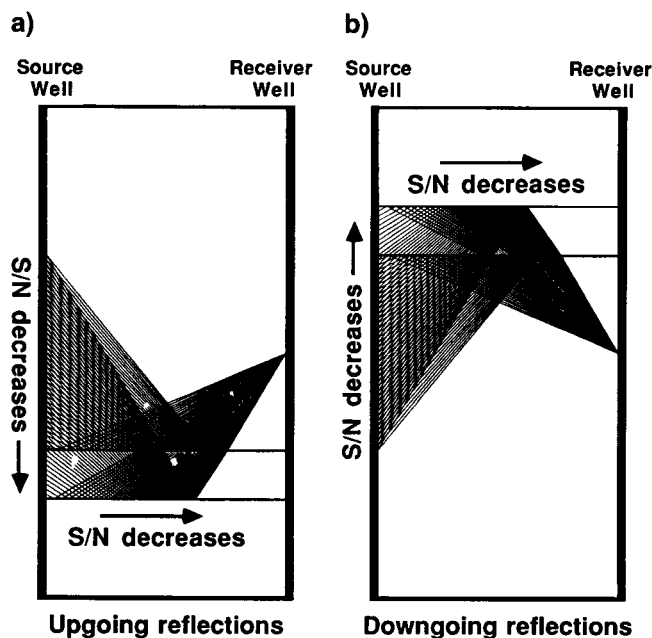


FIG. 9. Imaging with a common-receiver gather. The signal-to-noise ratio decreases as the reflection point moves away from the source well and also decreases for reflectors further away [deeper for upgoing (a), shallower for downgoing (b)] from the receiver.

mapping was the same one that was used for forward modeling (blocked sonic log). A 30-ft lateral mix was applied to the mapped result. The synthetic panel in Figure 10 is the first trace of the mapped, balanced, and mixed synthetic, repeated ten times.

Perhaps the most striking aspect of Figure 10 is the obvious difference in resolution between the synthetic for surface seismic frequencies and the cross-well reflection image. This difference is to be expected because of the widely different frequency bands of the two experiments. Surface seismic would be able to image the major contrasts—like the Eagle Ford shale interfaces or the gradational boundary at about 2250 ft (685 m)—but offers very little information about the finer scale [3–10 ft (1–3 m)] features indicated by the log. On the other hand, there is a large amount of information about these features contained in the cross-well reflected wavefield. At the wavelengths of investigation (a frequency of 2000 Hz corresponds to a wavelength of less than 7 ft (2 m) for the Austin chalk and less than 5 ft (1.5 m) for the Eagle Ford shale) even the finer features indicated by the well log have a detectable seismic response. This close correlation suggests that cross-well seismic data in this frequency range can bridge the resolution gap between surface seismic data and wireline logs and provide resolution down to a few feet.

In Figure 10 there is a small gap between the upper and lower parts of the cross-well reflection corridors. The upper

part was imaged with downgoing reflections, while the lower part was imaged with upgoing reflections. The gap between them corresponds to depths around the receiver depth where the incidence angles are extremely large. Such wide-angle reflections are difficult to preserve during wavefield separation and are unsuitable for reflection imaging. However, we still have kept reasonably wide angles in our image since incidence angles at the source well range from 50 to 80 degrees. For these data this was the range of angles for which the signal-to-noise ratio was acceptable. Yet, as a general statement, such wide-angle imaging is not desirable. Besides being difficult to reliably separate and image (very small errors in velocity produce large errors in depth for wide-angle reflections), wide-angle imaging drastically reduces lateral resolution. Also, for this range of angles, one will often have to deal with post-critical reflections. Rapid amplitude variations and phase shifts for incidence angles close to the critical angle would make interpretation of the images extremely difficult. In Figure 10, some of the events close to the receiver depth appear to be very strong, although they are not really produced by very big impedance contrasts. These large amplitudes are generated because of the extremely wide incidence angles. This is why one needs to compare the cross-well reflection images with synthetic data generated for the same range of incidence angles. We are so far away from normal incidence that regular zero-offset synthetics do not describe the physics of the experi-

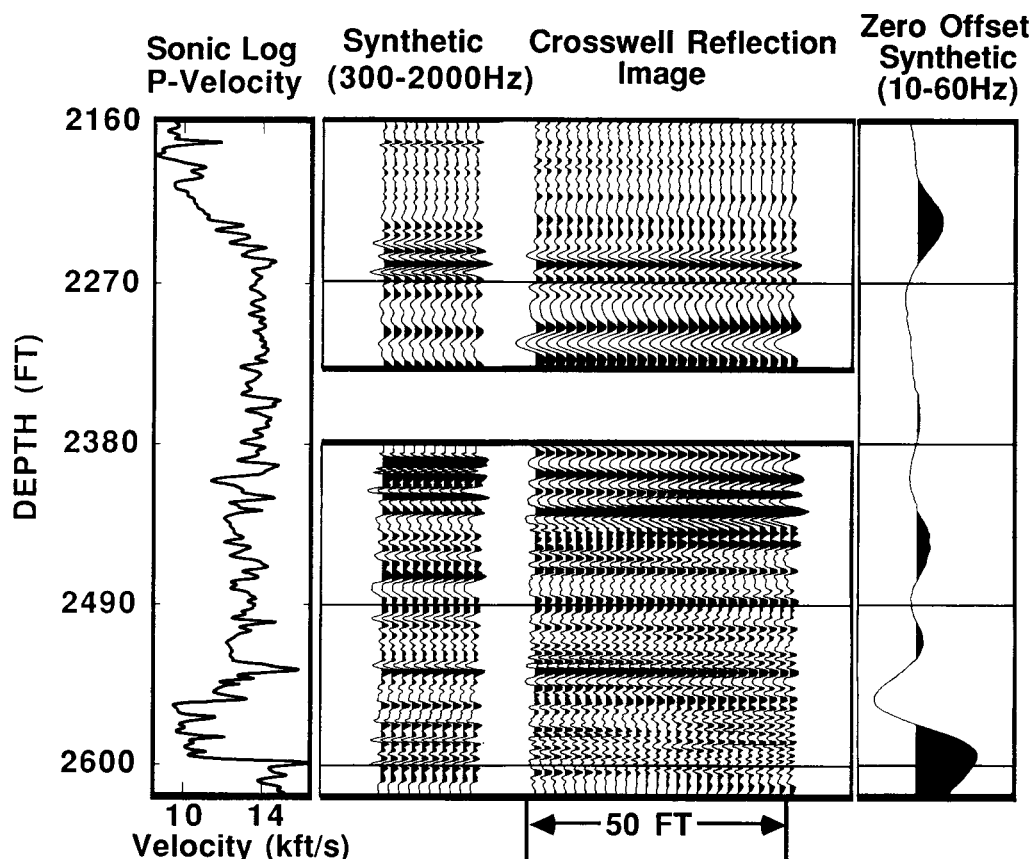


FIG. 10. Comparison of the cross-well reflection corridor to oblique-incidence (300–2000 Hz) and normal-incidence (10–60 Hz) synthetic seismograms.

ment. Even though we used an oblique incidence synthetic, you can notice that for the upper part of the lower corridor and the lower part of the upper corridor, the character of the synthetic response does not quite match the real data.

Even so, the tie between real and synthetic corridors is good for most of the depth range shown here, especially considering the original noisy nature of our data and the limitations of our processing due to the aliasing of the tube waves. Notice, for example, the excellent tie for the doublet at about 2490 ft (760 m) and the two of peaks following it—a sharp one followed by one less pronounced. The big peak at around 2540 ft (775 m) is also perfectly matched. This peak corresponds to the strong reflection that was visible even in the raw data (Figure 2). The next event, at a depth of around 2560 ft (780 m) is not perfectly matched, but we can at least identify its response in the real data. Notice also the sequence of reflections between about 2230 and 2280 ft (680 and 695 m), associated with the prominent peaks in the well log. The responses of the doublet at 2200 ft (670 m) and the peak at 2180 ft (665 m) are also well tied. The thicknesses of most of these features are less than 10 ft (3 m).

Overall, comparison between real and synthetic data shows good agreement for a large number of events. Although there are imperfections, the overall quality of the correlation provides convincing evidence that reflections exist in the cross-well wavefield and they can potentially be used for extremely high-resolution imaging.

Imaging away from the well

Let us now examine the result of imaging away from the source well. We explained before that as we move away from the source well, we effectively move away from the direct arrival and deeper into the data. As a consequence, the signal-to-noise ratio and the image quality degrade. This behavior is obvious when we look at Figure 11, which shows the result of imaging with only upgoing reflections. There is no lateral mix applied to this result. Obviously, this image is very noisy and unreliable. Although we can see events starting at the source well (the left side of the image), coherency is lost and interpretation becomes ambiguous as

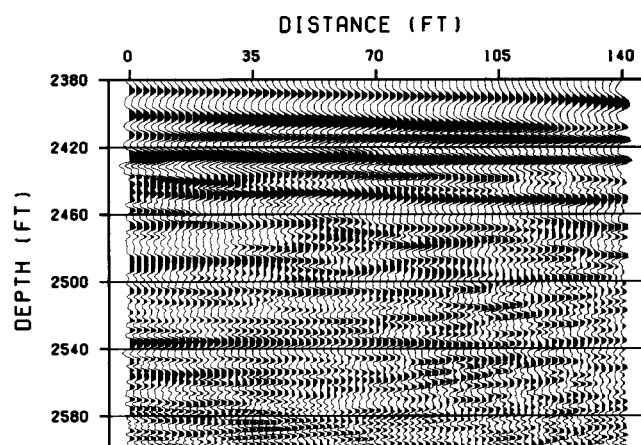


FIG. 11. Result of imaging with upgoing reflections. Horizontal distance is measured from the source well.

we move away from the well to the right part of the image. The strong reflection at 2540 ft (775 m) that was visible in the raw data can be seen to barely reach the right part of the image—140 ft (40 m) away from the source well—amid increasing levels of interfering noise. Other events, like the doublet at 2490 ft (760 m), can hardly be traced more than 50 ft (15 m) away from the source well. At about 2440 ft (745 m) we can see noise interfering with the reflection event even close to the well. As we move below the strong reflector at 2540 ft (775 m) and inside the Eagle Ford shale, the signal-to-noise ratio seems to decrease even more. This effect could be due to the fact that the big reflector at 2540 ft (775 m) is an efficient generator of tube waves. Strong tube waves originating at that depth can clearly be seen in Figure 4. Also, the impedance contrast that gives rise to the strong reflection at 2540 ft (775 m) creates, at the same time, significant transmission losses for energy propagating below it.

The top four events in this section seem to be strong and coherent all the way across the image. Their continuity is misleading though. Because of the way the XSP-CDP mapping works, these events experience a large horizontal stretch. For the lowest of these reflections [the one just below 2425 ft (740 m)], the part of the reflection event shown in the image is produced from about 5 traces of data, which, after mapping, are spread out to 25 image traces. This is a demonstration of the loss of lateral resolution that is a consequence of imaging with wide-angle reflections.

The result of imaging away from the well with downgoing reflections is shown in Figure 12a. This image looks less noisy than Figure 11. Again, this is partly caused by the fact that we are dealing with very wide angle, strong, possibly post-critical, reflections that look more continuous because they are highly stretched in the horizontal direction. The shallowest events in this section, corresponding to smaller incidence angles, are definitely less coherent. The most dominant feature in this figure is the large vertical stretch of the event at about 2300 ft (700 m), accompanied by rapid lateral variation in the reflection waveform. It is interesting that these effects are adequately simulated with the synthetic. Figure 12b shows the image that we get for the same interwell area when we map the synthetic data generated as described in the previous section. There is no lateral variation in the synthetic model, yet the mapped data show an effect similar to that in Figure 12a. The message conveyed by Figure 12 is that it could be very misleading to directly interpret images obtained from wide-angle reflections as indicative of the subsurface structure. Lateral variations observed in the section might be completely artificial and entirely due to the use of wide angles of incidence for imaging.

CONCLUSIONS

A number of significant conclusions can be drawn from the Devine case study. The most important points are summarized below.

- 1) Cross-well data contain reflections. These events are not always evident in the raw data because of the great variety of other events (direct arrival, source and receiver reverberations, multiples, conversions, source

and receiver well tube waves, etc.) that are also recorded. Yet they can be enhanced by appropriate processing and used for imaging. For the high frequencies produced by the piezoelectric bender, almost every impedance contrast shown in the well log produces a significant reflection. This is why reflection imaging holds the promise of very high resolution. We need not restrict ourselves to merely imaging the main geologic horizons. Cross-well reflections offer us a way to map the smaller-scale heterogeneities within the major units.

- 2) The application of VSP processing to cross-well data proved successful in enhancing the reflections. There are limitations to this approach though since the direct arrival does not provide a reliable estimate of the wavelet away from the well. Multiple elimination by deconvolution operators designed from the downgoing wavefield is not possible in the cross-well situation since both the upgoing and downgoing wavefields contain primaries and multiples.
- 3) Significant shear- and converted-wave energy exists in the piezoelectric bender wavefield and can potentially be used for multiple mode imaging. However, complete separation of compressional and shear waves might not be feasible with single-component data.
- 4) The piezoelectric bender, being a fluid-coupled down-hole source/receiver, generates strong tube waves. These events become a dominant source of coherent

noise that dominates almost everything in the wavefield except the direct arrival. Because tube waves have a well defined moveout that is usually different from the moveout of all events of interest, they can potentially be filtered out with multichannel filters, provided they are not aliased. Recording cross-well data so that the tube waves are not aliased for frequencies of a few kHz places a premium on efficient data acquisition.

- 5) Some of the strongest reflections present in cross-well data are wide-angle, post-critical reflections. Although these are strong events, they might not be appropriate for imaging. Images generated from such reflections might be misleading since they can exhibit severe horizontal and vertical stretching (compromising horizontal and vertical resolution) and rapid phase changes in the post-critical region.
- 6) Reflection processing and imaging of a single gather produced extremely high-resolution images near the well and a very good tie with the sonic log. However, images away from the well were very noisy and unreliable.

Although the good results close to the well are encouraging and suggest that cross-well reflection imaging might be feasible, the real objective of cross-well seismology is the imaging of heterogeneities away from the wells. This objective could not be achieved with the data used for this study. We should not forget, though, that the results shown here were produced from a single, significantly aliased gather. We should be able to produce much better results by using larger data volumes.

The wavefield should be sampled much more finely in space—meaning smaller depth intervals between source and receiver positions. For this experiment the 5-ft (1.5-m) spatial sampling created a Nyquist frequency of 475 Hz for the tube waves. With finer sampling, a larger part of the recorded spectrum would be unaliased.

Even if tube waves could be perfectly removed, a number of other sources of coherent noise—like shear and converted waves—would have to be dealt with. If we avoid using the very wide-angle, post-critical reflections, we are left with weaker reflections and a poorer signal-to-noise ratio. Given the complexity of the cross-well wavefield, it seems unlikely that single-fold images will be reliable. Similar to surface seismic, stacking multiple gathers is necessary for high-quality cross-well reflection imaging. Appropriate use of fold is not a trivial issue though, as the surface seismic experience suggests. Stacking high-frequency depth sections produced from wide-angle reflections is certainly a challenging problem. Yet, despite the anticipated technical difficulties, we believe that this study demonstrates the potential of cross-well reflection imaging for bridging the resolution gap between surface seismic data and wireline logs.

REFERENCES

- Abdalla, A. A., Stewart R. R., and Henley, D. C., 1990, Traveltime inversion and reflection processing of crosshole seismic data: 60th Ann. Internat. Mtg., Soc. Expl. Geophys., Expanded Abstracts, 47–50.
- Apsel, R. J., 1979, Dynamic Green's functions for layered media and applications to boundary-value problems: Ph.D. thesis, University of California at San Diego.

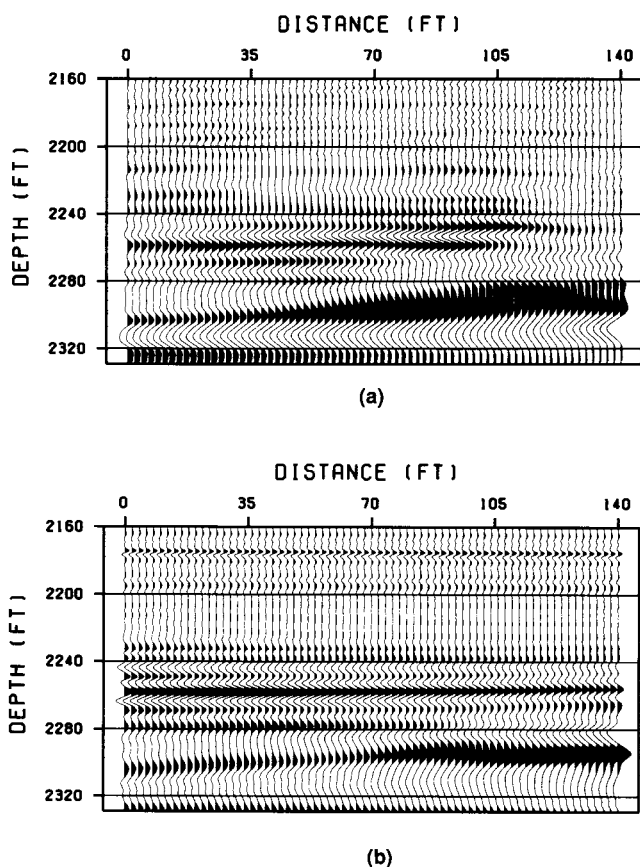


FIG. 12. Result of imaging with downgoing reflections. (a) Real data. (b) Synthetic data.

- Baker, L. J., and Harris, J. M., 1984, Cross-borehole seismic imaging: Presented at the 54th Ann. Internat. Mtg., Soc. Expl. Geophys.
- Balogh, T. W., Owen, T. E., and Harris, J. M., 1988, New piezoelectric transducer for hole-to-hole seismic applications: 58th Ann. Internat. Mtg., Soc. Expl. Geophys., Expanded Abstracts, 155-157.
- Becquey, M., Bernet-Rollande, J. O., Laurent, J., and Noual, G., 1991, Imaging reflectors in a cross-well seismic experiment: 53rd Ann. Internat. Mtg., Eur. Assn. Expl. Geophys., 152-153.
- Beydoun, W. B., Delvaux, J., Mendes, M., Noual, G., and Taran-tola, A., 1989, Practical aspects of an elastic migration/inversion of crosshole data for reservoir characterization: A Paris basin example: *Geophysics*, **54**, 1587-1595.
- Beydoun, W. B., and Mendes, M., 1989, Elastic ray-Born 12-migration/inversion: *Geophys. J.*, **97**, 151-160.
- Devaney, A. J., 1984, Geophysical diffraction tomography: *IEEE Trans. Geosci. Remote Sensing*, **GE-22**, 3-13.
- Hardage, B. A., 1985, Vertical seismic profiling, Part A: Principles, 2nd edition, Pergamon Press.
- Harris, J. M., 1987, Diffraction tomography with arrays of discrete sources and receivers, *IEEE Trans. Geosci. Remote Sensing*, **GE-25**, 448-455.
- 1988, Cross-well seismic measurements in sedimentary rocks: 58th Ann. Internat. Mtg., Soc. Expl. Geophys., Expanded Abstracts, 147-150.
- Hu, L., McMechan, G. A., and Harris, J. M., 1988, Acoustic prestack migration of cross-hole data: *Geophysics*, **53**, 1015-1023.
- Iverson, W. P., 1988, Cross-well logging for acoustic impedance: *Pet. Tech. J.*, vol. 40, 75-82.
- Lee, M., and Balch, A., 1982, Theoretical seismic wave radiation from a fluid-filled borehole: *Geophysics*, **47**, 1308-1314.
- Lo, T. W., Toksöz, M. N., Xu, S., and Wu, R. S., 1988, Ultrasonic laboratory tests of geophysical tomographic reconstruction: *Geophysics*, **53**, 947-956.
- Miller, D. E., and Chapman, C. H., 1991, Incontrovertible evidence of anisotropy in cross-well data: 61st Ann. Internat. Mtg., Soc. Expl. Geophys., Expanded Abstracts, 825-828.
- Miller, D., Oristaglio, M., and Beylkin, G., 1987, A new slant on seismic imaging: Migration and integral geometry: *Geophysics*, **52**, 943-964.
- Onishi, M., and Harris, J. M., 1991, Anisotropy from head waves in cross-well data: 61st Ann. Internat. Mtg., Soc. Expl. Geophys., Expanded Abstracts, 115-118.
- Pratt, R. G., and Worthington, M. H., 1990a, Inverse theory applied to multisource crosshole tomography. Part 1: Acoustic wave-equation method: *Geophys. Prosp.*, **38**, 287-310.
- 1990b, Inverse theory applied to multisource crosshole tomography: Part 2: Elastic wave-equation method: *Geophys. Prosp.*, **38**, 311-329.
- Rector, J. M., Lazaratos, S. K., Harris, J. M., and Van Schaack, M., 1992, Spatial sampling of cross-well wavefields: 54th Ann. Internat. Mtg., Eur. Assn. Expl. Geophys., 592-593.
- 1994, Wavefield separation of cross-well seismic data: Scheduled for publication in January 1994 *Geophysics*.
- White, J. E., 1983, *Underground sound*: Elsevier Science Publ. Co. Inc.
- Woodward, M. J., 1989, Wave-equation tomography: Ph.D. thesis, Stanford Univ.
- Wu, R. S., and Toksöz, M. N., 1987, Diffraction tomography and multisource holography applied to seismic imaging: *Geophysics*, **52**, 11-25.
- Wyatt, K. D., and Wyatt, S. B., 1984, Determining subsurface structure using the vertical seismic profiling, in Toksöz, M. N., and Stewart, R. R., Eds., *Vertical seismic profiling: Advanced Concepts*, Geophysical Press., 148-176.

